



Interfacial engineering enables polyaniline-decorated bismuth sulfide nanorods towards ultrafast metal–semiconductor-metal UV-Vis broad spectra photodetector

Anshika Singh^{1,3} · Pratima Chauhan¹ · Arpit Verma² · Bal Chandra Yadav²

Received: 23 March 2023 / Revised: 15 March 2024 / Accepted: 22 March 2024 / Published online: 8 May 2024
© The Author(s), under exclusive licence to Springer Nature Switzerland AG 2024

Abstract

Herein, we reported photoelectric measurements of the polyaniline decorated with bismuth sulfide ($\text{Bi}_2\text{S}_3/\text{PANI}$) nanohybrid based metal-semiconductor-metal (MSM) device in the broad electromagnetic (EM) spectrum from ultraviolet (UV) to visible (Vis) range. Bi_2S_3 nanorods decorated with π -conjugated polymer PANI were utilized as photodetection devices has a wide range of applications in imaging and communication. In such a novel structure, the fast electron transfer at the interface of Bi_2S_3 and PANI occurs, which enhances the performance of the photodetectors. Current–voltage (I – V) characteristics of the MSM photodetector device of $\text{Bi}_2\text{S}_3/\text{PANI}$ nanohybrid show good ohmic nature. This photodetector device offers the highest external quantum efficiency (EQE) 10⁴% in the UV and visible regions. It also shows the greatest detectivity of the order 10¹⁴ Jones. The photoresponsivity of the $\text{Bi}_2\text{S}_3/\text{PANI}$ nanohybrid photodetector device shows 270 mA W^{-1} in UV region and 1270 mA W^{-1} in visible region at only 1 V with the minimum optical signal of 50 $\mu\text{W cm}^{-2}$. The highest photoresponsivity of the $\text{Bi}_2\text{S}_3/\text{PANI}$ nanohybrid photodetector offers 26,760 mA W^{-1} and 13,250 mA W^{-1} for the UV and visible spectra, respectively. The higher values of the LDR are 64.31 dB and 58.21 dB in the UV and visible regions, respectively, at 100 V with the lowest illumination intensity. The minimum value of NEP found in the order of 10^{−9} W which is the lowest value, suggests that the nanohybrid material is perfect for low-intensity photon signals. This work provides simple and effective method for the preparation of MSM photodetector technology exhibits a magnificent performance in the UV-to-Vis region.

Keywords Bismuth sulfide · Metal–semiconductor-metal device · Conjugated polymer polyaniline

1 Introduction

Bismuth sulfide (Bi_2S_3) is a semiconductor with a lamellar structure whose direct band gap E_g is 1.3 eV. Bi_2S_3 has recently gained interest as a potential functional material for various applications, including thermoelectric, photodetectors, and solar cells [1–6]. It takes advantage of exciting features like a favorable band gap, a high absorption coefficient, and environmentally

friendly elements [7, 8]. The van der Waals forces hold together the orthorhombic crystal structure of stoichiometric Bi_2S_3 and have a layered structure in atomic-scale ribbons. The production of one-dimensional (1D) nanostructures, including nanoflowers [2, 9], nanowires [7, 8, 10], rods [1, 11, 12], tubes, and ribbons, is encouraged by the structure of Bi_2S_3 [1]. Co-nucleus growth was used to generate the 1D nanowires on a monolayer of MoS_2 , creating platforms with great promise for optoelectronic applications [7, 12]. Additionally, 2D Bi_2S_3 nanosheets and colloidal quantum dots (CQDs) have been synthesized. Although photodetectors based on Bi_2S_3 nanomaterials have been described, they perform inferior commercial silicon detectors and recently developing material platforms, including 2D materials [13], perovskite, and QD-based hybrid photodetectors. Until now, semiconductor excitation with photon energy at least equivalent to their band gap has been the basis for high-performance photodetectors. Therefore, selecting a semiconductor material to address a specific spectral band has been a determinant factor. Technologies for detecting light in the UV or visible spectrum include biological imaging, artificial intelligence, chemical sensing, environmental monitoring, missile launching, and

✉ Anshika Singh
anshikasinh@allduniv.ac.in; dranshika23@gmail.com

✉ Pratima Chauhan
mangu167@yahoo.co.in

¹ Advanced Nanomaterials Research Laboratory, U.G.C. Centre of Advanced Studies, Department of Physics, University of Allahabad, Prayagraj, Uttar Pradesh, India

² Nanomaterials and Sensors Research Laboratory, Department of Physics, Babasaheb Bhimrao Ambedkar University, Lucknow, Uttar Pradesh, India

³ Present Address: SAMTEL Centre for Display Technologies, Indian Institute of Technology Kanpur, Kanpur, Uttar Pradesh, India

optical communication [14–19]. Commercial photodetectors are made of silicon (Si) and silicon carbide (SiC) for detection in the visible and UV spectral regions. Developing a single, inexpensive, multi-spectral photodetector that can work at room temperature and in the visible and UV spectral bands is very desirable [20, 21].

Many types of photodetectors have been created, but organic–inorganic hybrid photodetectors (OIHPDs) have garnered much attention lately. Unlike other types of photodetectors, OIHPDs have both the advantages of organic-based devices, such as functional tunability and ease of formation [22], as well as the characteristics of inorganic-based devices, such as broadband absorption and excellent intrinsic carrier mobilities [23–26]. Furthermore, the remarkable reaction at the interface between organic polymers and inorganic semiconductors is advantageous for photoconductive applications [15, 27, 28]. Photodetectors (PDs) are a vital part of daily life, from essential automatic lighting in the hallways of our buildings to cruise control in automobiles [29–31]. Fast detection of weak signals is frequently necessary, and inorganic avalanche photodiodes currently provide this service. As the automotive sector transitions to self-driving cars, qualities including increased sensitivity, cheaper cost, wavelength selectivity, and form-free devices are necessary [16, 30, 32]. These characteristics can be found in PDs made of organic semiconductors, but further study is required to tune the devices for low-intensity signals and achieve high specific detectivities [16]. In recent years, there has been increased interest in studies on organic photodetectors (OPDs) with high sensitivity and integration [33, 34]. OPDs can be divided into two categories according to their operational principles: photodiode type with EQE values below 100% and photomultiplication (PM) type EQE values above 100%. The photon harvesting, charge separation, transport, and collecting efficiencies all play a role in determining the EQE of OPDs [33, 34]. PM can be produced in nanohybrid materials using various techniques, such as co-planar structures with or without trap-assisted injection and sandwich structures with charge carrier tunneling injection [21, 35–37]. In nanohybrid materials, opposing charge carriers travel through the active layer and are driven to the appropriate electrode where photo-generated electrons or holes are trapped or hindered [37]. Nanohybrid photodetectors with limited dark current exhibit high EQE values because there are no continuous electron transport channels in the active layers and a relatively high Schottky barrier for hole injection. These organic semiconductors are π -conjugated conducting polymers and tiny organic compounds. Organic semiconducting polymers such as polyaniline [34, 38–40], polypyrrole [41], polythiophene [42], poly(3-hexylthiophene-2,5-diyl) [43], and poly(3,4-ethylenedioxythiophene)-poly(styrenesulfonate) [15] have been reported for photodetectors. The superior solution

processability and readily tunable characteristics of organic semiconductors producing flexible, inexpensive, and thermally efficient photodetectors possible. Polyaniline (PANI) is an exception among various conducting polymers due to its remarkable attributes and extensive research focus. Its reversible doping/de-doping behavior, outstanding electrical conductivity, high charge storage capacities, and environmental stability make it particularly significant. The alternating single and double bonds within the PANI chain facilitate electron conduction, leading to diverse applications such as electromagnetic shielding [44–47], and electrode material for batteries and supercapacitors [48] as well as sensors [49, 50]. The electrical conductivity of doped PANI can be finely adjusted, with different dopants enabling conductivity enhancements of 8–11 orders of magnitude compared to undoped PANI [51]. Moreover, the quantity and dimensions of dopants play a crucial role in shaping the morphology of PANI [34, 52]. However, because p-electrons serve as the source of carriers, organic semiconductors often have limited charge carrier mobility. The performance of the devices are greatly hampered by low mobility. Combining hybrid organic–inorganic junctions is a highly desired and promising strategy to get beyond the limits of both organic and inorganic semiconductors. Recently, M. Rabia et al. reported Ppy/Ni(OH)₂-NiO nanocomposites for photoresponse properties showed photoresponsivity 12.50 mA W⁻¹ while the detectivity is 2.79 × 10¹¹ Jones [41]. B. Karthikeyan reported the ternary nanocomposite of ZnO@MOS₂ core–shell heterostructures with PANI photodetector exhibits a photoresponsivity of 79.60 mA W⁻¹ and a detectivity of 1.43 × 10⁸ Jones [53]. Coupling organic and inorganic semiconductors is the best way to create inexpensive, flexible, and low-temperature processed photodetectors since their qualities complement one another. High spectral responsiveness and fast reaction times are generally desired in devices like spectrophotometers and light meters, cameras, and mobile phones, and in a variety of industries, including remote sensing, optical communication, defense equipment, night-vision, and process monitoring. Photodetectors are implemented in various topologies, including metal–semiconductor junctions, photodiodes, phototransistors, and photoresistors [36, 54–57]. Devices based on these traditional semiconductors require difficult production conditions and significant thermal losses despite their superior performance. Due to these problems, research interest in new materials that could replace these conventional semiconductors and cleanroom-free manufacturing methods for flexible photodetectors is booming. Inorganic semiconductors have more significant optical absorption coefficients and mobility, and their optical characteristics may be significantly altered by doping, stoichiometry control, size tuning, and strain engineering [26]. However, they have low solution processability, high manufacturing costs, a need

for high temperatures during device construction, and poorer compatibility with lightweight materials [35, 58]. A vertical type NGQDs/CsPbBr₃ heterostructure photodetector showed responsivity 3.21 AW⁻¹, specific detectivity 2.90 × 10¹² J, and an EQE 270% under the illumination of a light source with a wavelength of 520 nm and power intensity of 0.80 mWcm⁻² at a bias voltage of 3 V [24]. The exceptional alignment of the MoS₂, NH₂ GQDs, and CsPbBr₃ allowed the triple junction to decrease recombination and increase photon-absorption rate, which improved the hybrid PD's performance.

Considering the advantages, numerous OIHPD prototypes have been published and described for their optoelectronic characteristics as tabulated in Table 1. 1D nanostructures feature have many surface trap states because of their vast aspect ratio and high surface-to-volume ratio, which can extend carrier lifetimes. 1D nanostructure-based photodetectors have excellent responsivity and photoconductive gain due to the low dimensionality of these structures, which can also shorten transit times and constrain the effective area of charge carriers. The best option for integrating the remarkable benefits of 1D nanostructures with the plentiful trap states of organic–inorganic interfaces is organic–inorganic hybrid nanorods (NRs). Incorporating Bi₂S₃ into a polymer matrix expands its capabilities, facilitating charge transfer, electronic interactions, and morphological adjustments. These alterations enhance the properties of the hybrid material, rendering it more cost-effective. The comparative analysis of the previously reported organic–inorganic nanohybrid photodetectors (OINPDs) with this work is shown in Table 1.

Additionally, compared to two- (2D) and three-dimensional (3D) nanostructures, a 1D organic–inorganic hybrid NR is the best dimension for exploring the mechanism for efficient carrier transport. Due to its controlled shape and excellent purity, a hydrothermal method was used in this work to examine the Bi₂S₃ material. The optimized chemical oxidative polymerization was used to develop the π -conjugated polymer polyaniline decorated bismuth sulfide (Bi₂S₃/PANI) hybrid system for UV-Vis broadband photodetectors.

2 Experimental section

2.1 Materials

Bismuth nitrate (Bi(NO₃)₂·5H₂O > 99%), thiourea (CH₄N₂S > 99.1%), ethylene glycol (C₂H₆O₂ > 99.3%), aniline (C₆H₅NH₂ > 99.5%), hydrochloric acid (HCl), and ammonium peroxy-di-sulfate ((NH₄)₂S₂O₈ > 99%) were purchased from Merck India. All the chemicals were used as procured without any further purification process.

2.2 Synthesis of Bi₂S₃

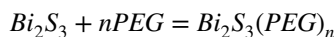
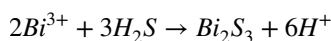
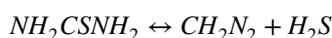
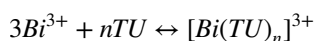
50 mL of ethylene glycol (EG) was initially used to dissolve 2 mmol of Bi(NO₃)₂·5H₂O while mechanically stirring for 30 min. After the Bi(NO₃)₂·5H₂O solution had dissolved entirely, 2 mmol of thiourea was added to ensure homogeneity for 30 min. The mixture was then sealed inside a 250-ml

Table 1 Comparative analysis of the qualitative parameters of the photodetector devices

Materials	Photodetection range	Rise/decay time	Responsivity (mA W ⁻¹)	Detectivity (Jones)	EQE (%)	Ref
GaN/PANI	UV	1.1/1.8 ms	69	8.45 × 10 ¹³	26	[59]
NZF-PANI	Visible	0.9/0.8 s	24.98	3.7354 × 10 ¹²	-	[33]
Se/PANI	Visible	4.50/2.84 ms	120	3.78 × 10 ¹¹	-	[60]
Se/PPY		0.35/16.97 ms	70			
Se/PEDOT		1.00/9.78 ms	5.5			
WSe ₂ -PANI	Visible	0.9/1 s	9	5.8 × 10 ⁹	-	[61]
TiO ₂ /PC71BM/PEDOT:PSS	UV	60 ms/ < 1 μ s	33	1.60 × 10 ¹¹	-	[62]
Ga ₂ O ₃ /PANI	UV	0.34/8.14 ms	21	1.50 × 10 ¹¹	-	[63]
CuBi ₂ O ₄ -PANI	UV	1.35/0.97 s	5.38	6.016 × 10 ¹¹	1.824 × 10 ³	[34]
SnSe ₂ /PEDOT: PSS	UV	16 ms	730	-	-	[15]
	Visible	221 ms	690			
	NIR	274 ms	670			
ZnS/PANI	UV	-	396.47	1.68 × 10 ¹³	1.34 × 10 ⁵	[40]
TiO ₂ /PANI	UV	3.8/30.7 ms	3.6	3.9 × 10 ¹¹	-	[64]
MgZnO/PANI	UV	4.8/5.1 ms	0.16 × 10 ⁻³	1.5 × 10 ¹¹	-	[38]
Bi₂S₃/PANI	UV	50/63 ms	26,760	5.24 × 10¹³	9073	This work
	Visible		13,250	2.59 × 10¹³	4493	

Bold entries indicates present work

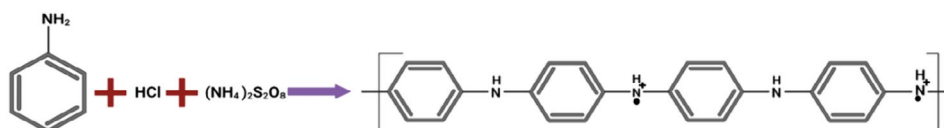
Teflon container. The reactant-filled Teflon cylinder was closed before being placed into a stainless-steel chamber. A tight screw was used on the stainless-steel cap to prevent solvent loss at temperature. Following that, the vessel was held at 200°C for 24 h. All reactions were accomplished at the pre-determined temperature and duration. Then, the container was gradually air-cooled to room temperature. To get rid of unreacted compounds like EG and clear the solvent residue from the surface of the material, the products were centrifuged and washed many times with distilled water and dehydrated ethyl alcohol. The material yielded excellent after drying at 80°C in a Bi₂S₃ black precipitate for 2 h. The formation of the Bi₂S₃ is understood by the given reaction below:



2.3 Synthesis of Bi₂S₃/PANI

In this process, the solvent medium for the polymerization of aniline (C₆H₅NH₂) monomer was prepared by mechanically agitating 1 M HCl into 40 ml DI water for 15 min. After that, 1 M C₆H₅NH₂ monomer and 0.1 g Bi₂S₃ were added to the solvent while the mixture was mechanically stirred for 20 min. Following this, the mixture was mechanically agitated for a further hour while 0.8 M of ammonium peroxy-di-sulfate (APS) was an initiator in the polymerization process and dissolved in 40 ml of DI water. The mixture was then placed in a 250-ml Teflon autoclave and heated to 80°C for 6 h. A dark green precipitate was gathered, cleaned with HCl and DI water, and dried at room temperature. The polymerization reaction of the aniline monomer into polyaniline is given in Fig. 1. Two other nanohybrid samples of Bi₂S₃/PANI were also prepared using 0.8 M and 0.6 M concentrations of the aniline monomer synthesized by the same method as described above.

Fig. 1 The chemical oxidation polymerization reaction for the aniline monomer into the polyaniline chain



2.4 Fabrication of the photodetector device

A metal–semiconductor–metal (MSM) photodetector device based on a Bi₂S₃/PANI nanohybrid was fabricated on a fluorine doped tin oxide (FTO) substrate with two co-planar metal contacts of silver (Ag/nanohybrid/Ag). A total of 0.1 g of Bi₂S₃/PANI nanohybrid material was dissolved in 5 ml dimethyl sulfoxide (DMSO) and ultrasonicated for 1 h. After that, the solution was used to spin-coat on the 0.5 × 0.5 cm² FTO substrate at 2000 rpm and then dried at 50°C. Now, the prepared solution-processed Bi₂S₃/PANI nanohybrid material based device was used for the photodetection measurements with an electrode spacing of 1 mm with 4 mm² active area of the device and the silver paste was used for the electrode. The photodetection setup consists of a Keithley electrometer system, a data collection system, and two light sources, one with a wavelength centered in the UV area of 365 nm and other in the visible range of 550 nm.

3 Results and discussion

3.1 Structural analysis

Structural analysis of the pristine Bi₂S₃ and Bi₂S₃/PANI nanohybrid samples were carried out by the X-ray diffraction (XRD). The XRD pattern of the Bi₂S₃ perfectly matches well with the standard diffraction pattern of the pure primitive orthorhombic phase of the Bi₂S₃ (JCPDS number 17–0320). The XRD pattern of the hybrid Bi₂S₃/PANI shows a broad peak at 2θ = 25°, indicating the presence of PANI in the hybrid system, and the other peaks ideally meet with the Bi₂S₃ as shown in Fig. 2. The hydrothermal treatment of Bi₂S₃/PANI nanohybrids leads to a reduction in XRD peaks associated with PANI within the hybrid system. This process promotes the chemical bonding of PANI chains with Bi₂S₃, thereby facilitating the transfer of charge carriers within the photodetector device. The structural analysis of the prepared samples were confirmed through the XRD pattern of the Bi₂S₃ and Bi₂S₃/PANI nanohybrids.

3.2 Surface morphological and compositional analysis

The surface morphological analysis of the pristine Bi₂S₃ and Bi₂S₃/PANI nanohybrid samples were carried out by

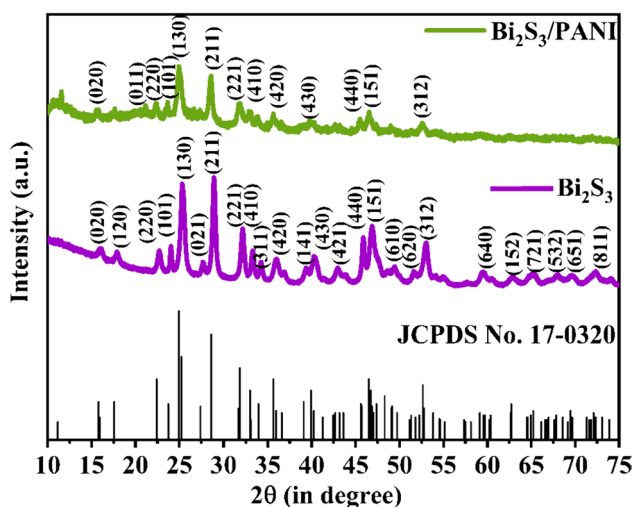


Fig. 2 X-ray diffraction pattern of the pristine Bi_2S_3 and $\text{Bi}_2\text{S}_3/\text{PANI}$ nano hybrid samples

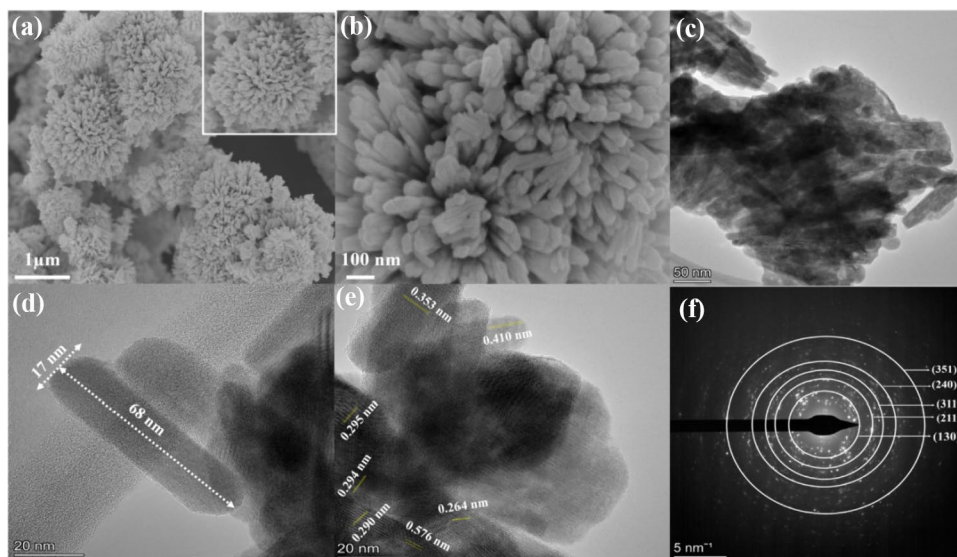
field emission scanning electron microscopy (FE-SEM). FE-SEM micrographs of the Bi_2S_3 sample in Fig. 3a show hierarchal nanoflower like structures at 1 μm , and Fig. 3b shows nanorods assembled in the form of a flower structure as indicated at 100 nm. Scanning electron microscopy (SEM) was also used for the morphological analysis of the as synthesized Bi_2S_3 material shows foam like spherical structures, as shown in Fig. S1. The TEM micrograph of the $\text{Bi}_2\text{S}_3/\text{PANI}$ sample at 50 nm shows Bi_2S_3 nanorods intercalated in the PANI matrix, as shown in Fig. 3c. It shows distortion of Bi_2S_3 hierarchal flower into nanorods, due to the use of acidic solution in oxidative chemical polymerization of polyaniline. High-resolution transmission electron microscopy (HR-TEM) was used to determine the crystallographic structures of the

materials at the atomic scale. The HRTEM imaging of the $\text{Bi}_2\text{S}_3/\text{PANI}$ clearly shows nanorods of the length 68 nm and width of 17 nm at the scale 20 nm as shown in Fig. 3d. The interplanar spacing was also estimated through the HR-TEM image, which is mentioned in the picture at 20 nm in Fig. 3e. The selected area electron diffraction (SAED) pattern of the $\text{Bi}_2\text{S}_3/\text{PANI}$ sample was well matched with the XRD pattern of the pristine Bi_2S_3 , as shown in Fig. 3f.

The elemental composition of the materials were determined using the surface-sensitive quantitative spectroscopy method known as X-ray photoelectron spectroscopy (XPS). When a material is exposed to an X-ray beam for analysis, the kinetic energy and quantity of escaping electrons from the top 10 nm from the surface of material are concurrently counted and measured to produce an XPS spectrum. It investigates elements in a material's compositional structure, empirical formula, and chemical and electronic state. De-convolution of the core spectra of all the components was done using the Lorentzian fitting. The XPS survey spectrum of the $\text{Bi}_2\text{S}_3/\text{PANI}$ nano hybrid material as shown in Fig. 4a. In the $\text{Bi}_2\text{S}_3/\text{PANI}$ nano hybrid material, the core spectrum of the bismuth (Bi) element in which Bi 4f doublets and S 2p doublet inside the Bi 4f doublet gap are observed is shown in Fig. 4b. The prominent peaks at 158.41 and 163.70 eV are attributed to Bi 4f_{7/2} and Bi 4f_{5/2} for Bi^{3+} states, respectively. The accompanying weak Bi 4f doublet at lower energy (157.11 and 162.40 eV for Bi 4f_{7/2} and Bi 4f_{5/2}, respectively) is assigned to under-coordinated and reduced Bi species with lower valency, Bi^{2+} according to previous reports, suggesting the existence of sulfur vacancies in pristine samples [50, 65, 66].

Moreover, the separation between Bi 4f_{7/2} and Bi 4f_{5/2} was 5.31 eV, indicating a characteristic Bi^{3+} state. The core spectrum of sulfur (S) shows binding energy with 165.77 eV and

Fig. 3 a FE-SEM micrograph at 1 μm , b FE-SEM micrograph at 100 nm, c TEM micrograph at 50 nm, d HRTEM image of a nanorod at 20 nm, e HRTEM image at 20 nm, f SAED pattern of the $\text{Bi}_2\text{S}_3/\text{PANI}$



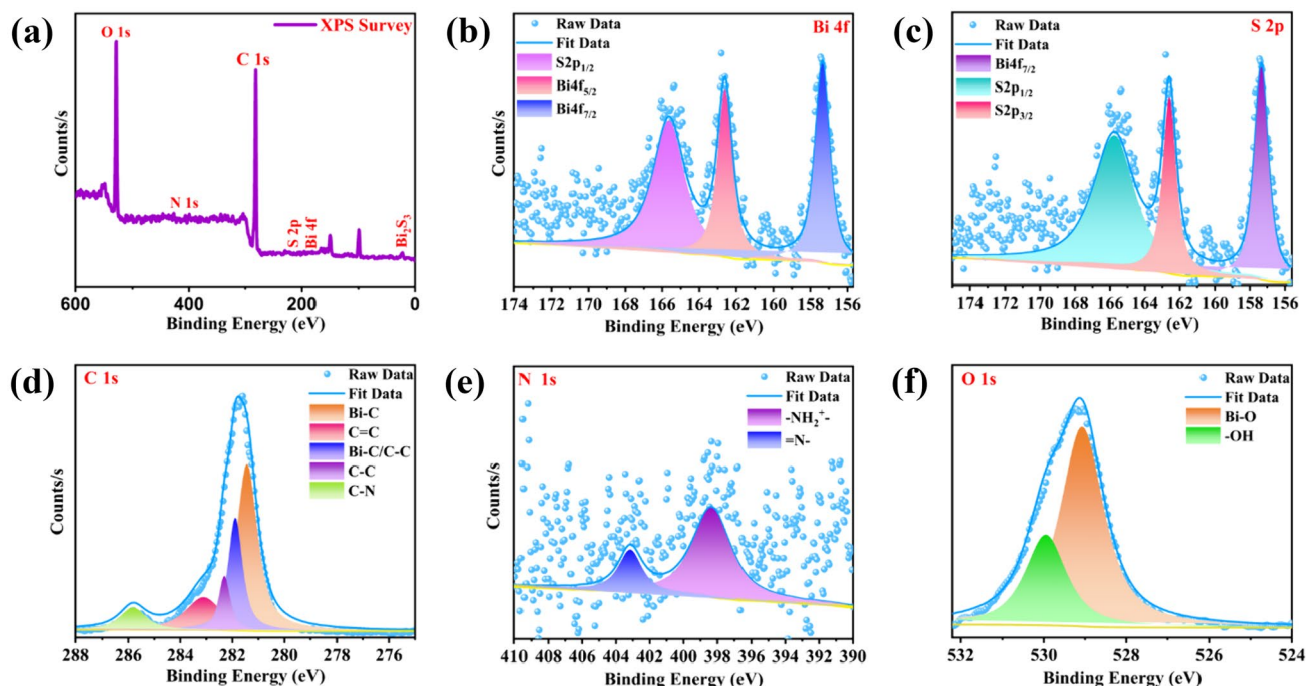


Fig. 4 XPS survey of **a** $\text{Bi}_2\text{S}_3/\text{PANI}$ nanohybrid; core spectra of **b** Bi 4f spectra, **c** S 2p spectra, **d** C 1s spectra, **e** N 1s spectra, and **f** O 1s spectra of the $\text{Bi}_2\text{S}_3/\text{PANI}$ nanohybrid

162.57 eV for S $2p_{1/2}$ and S $2p_{3/2}$, respectively, as shown in Fig. 4c. The core spectrum of carbon (C) shows binding energy of 285.78 eV for C-N, 283.13 eV for C=C, 282.31 eV for C-C, 281.90 eV for Bi-C or C-C, and 281.44 eV for Bi-C in the $\text{Bi}_2\text{S}_3/\text{PANI}$ nanohybrids. This outcome provides more evidence of the presence of Bi-C in the $\text{Bi}_2\text{S}_3/\text{PANI}$ nanohybrids. As mentioned in the literature, the Bi-C bond in the $\text{Bi}_2\text{S}_3/\text{PANI}$ nanohybrid can serve as a quick electron transfer channel as depicted in Fig. 4d. The core spectrum of nitrogen (N) shows 403.15 eV and 398.34 eV for $-\text{NH}_2^+$ and $=\text{N}-$, respectively, as represented in Fig. 4e. The core spectrum of oxygen (O) shows a binding energy of 529.93 for $-\text{OH}$ and 529.06 for Bi-O as displayed in Fig. 4f. The interaction of the PANI confirmed with the Bi-C bond in the $\text{Bi}_2\text{S}_3/\text{PANI}$ nanohybrid. Additionally, Bi_2S_3 is coupled to carbon via a chemical bond called a Bi-C bonding; the schematic illustration of the electron transport characteristics in $\text{Bi}_2\text{S}_3/\text{PANI}$ is displayed. Bi-C bonds and highly conductive polymers in such a new structure should facilitate electron transport while preserving structural integrity during photodetection.

3.3 Optical analysis

Furthermore, we have carried out the Fourier transform infrared (FTIR) spectral analysis over the range of $4000\text{--}500\text{ cm}^{-1}$ to investigate the functional groups associated with the vibrational modes in PANI and to better comprehend its chemical interactions with Bi_2S_3 nanoflowers in the $\text{Bi}_2\text{S}_3/\text{PANI}$ nanohybrid. The distinctive FTIR spectra of PANI, Bi_2S_3 , and $\text{Bi}_2\text{S}_3/\text{PANI}$

nanostructures are given in Fig. 5. The characteristic absorbance peaks at 446 cm^{-1} , 737 cm^{-1} , and 865 cm^{-1} are attributed to the Bi-S interaction and shifted to 745 cm^{-1} and 869 cm^{-1} in $\text{Bi}_2\text{S}_3/\text{PANI}$ [50, 65, 66]. The peak observed at 977 cm^{-1} is due to resonance interaction between vibrational modes of sulfur ions and shifted to 981 cm^{-1} in the $\text{Bi}_2\text{S}_3/\text{PANI}$ [66]. The peaks observed at 1201 cm^{-1} , 1396 cm^{-1} , and 1550 cm^{-1} correspond to the charge delocalization and shifted to 1226 cm^{-1} ,

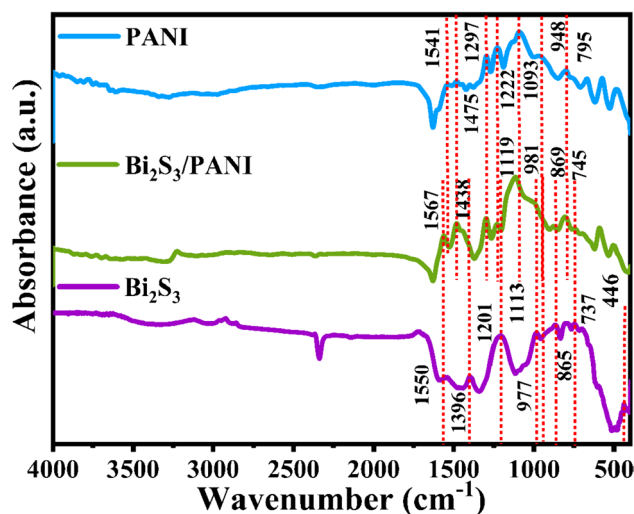


Fig. 5 Fourier transform infrared spectra (FTIR) of PANI, $\text{Bi}_2\text{S}_3/\text{PANI}$, and Bi_2S_3

1433 cm^{-1} , and 1567 cm^{-1} in the $\text{Bi}_2\text{S}_3/\text{PANI}$ [66]. The band observed at 948 cm^{-1} is attributed to the N-H^+ group present in the PANI chain, while the peak at 1475 cm^{-1} is assigned to C–N stretching vibrations and suggests the development of $[\text{Bi}(\text{TU})_x]^{3+}$ complex (TU is thiourea) in the Bi_2S_3 nanoflowers. The observed changes in the FTIR spectra of Bi_2S_3 -doped nanohybrids are mostly around C–N stretching, suggesting substantial coupling/interactions between the Bi_2S_3 crystallites and the imine nitrogen in the conducting polymer [65]. The characteristic peaks of PANI at 795 cm^{-1} are assigned to the C–H bonding mode of aromatic rings, 1093 cm^{-1} is due to the C–H bonding of benzenoid units, 1222 cm^{-1} is due to the N=Q=N stretching mode of quinoid (Q) rings, 1297 cm^{-1} corresponds to C=N , 1475 cm^{-1} is assigned to C–N stretching of benzenoid rings, and 1541 cm^{-1} to C–N stretching of quinoid units suggesting the formation of emeraldine base form of PANI [53, 66]. It is believed that there was substantial chemical contact and potential charge transfer between Bi_2S_3 and PANI, which caused the observed shift of their peaks in the $\text{Bi}_2\text{S}_3/\text{PANI}$ nanocomposite. The corresponding peaks of both Bi_2S_3 and PANI in the FTIR spectrum of $\text{Bi}_2\text{S}_3/\text{PANI}$ verify their presence in the nanohybrid sample.

UV visible spectroscopy of Bi_2S_3 and $\text{Bi}_2\text{S}_3/\text{PANI}$ nanohybrid samples was observed in the range of the 195 to 1100 nm region, as shown in Fig. S2. The pristine Bi_2S_3 sample had a broad absorbance peak between 600 and 800 nm. The absorbance peak in the $\text{Bi}_2\text{S}_3/\text{PANI}$ nanohybrid was moved to the lower wavelength side after the Bi_2S_3 was conjugated with the PANI matrix. The material's optical band gap (E_g) is determined by plotting the graph between $h\nu$ and $(\alpha h\nu)^2$. The optical band gap of the material is estimated by Eq. (1):

$$\alpha h\nu = A(h\nu - E_g)^n \quad (1)$$

where ν is the transition frequency, A is constant, and $n=0.5$ (for direct band gap). The straight-line portion of the plot was extrapolated to the x -axis, which gives the optical band gap of the Bi_2S_3 and $\text{Bi}_2\text{S}_3/\text{PANI}$ found to be 1.13 eV and 1.50 eV, respectively.

3.4 Electrical measurements of $\text{Bi}_2\text{S}_3/\text{PANI}$ nanohybrid as photodetector

In the photodetection process, photons are absorbed in the semiconductor, leading to the generation of electron–hole (e–h) pairs. A semiconductor participates in photogeneration when it is stimulated by the light of specific wavelength; if $h\nu$ or the energy of the light is larger than the semiconductor's band gap, then one electron jumps from the valence band (VB) to the conduction band (CB), producing an e–h pair. When the absorbing light of energy $h\nu > E_g$, electrons from the VB go to the CB, leaving a hole in the valence band.

The thermionic theory is the basis for the current transport mechanism in the MSM device topologies. Photoconductors and photodiodes are the two different categories of PDs. The EQE of photodiodes is typically less than 1 due to inadequate light absorption, carrier recombination, and other factors. Still, the response is quick because both electrons and holes are engaged in photocurrent generation and recombination after reaching their electrodes with transient carrier lifetimes. A photoconductor traps the other sort of carrier, which is used to generate the photocurrent. The carrying carriers have a high responsiveness but a long reaction time due to their ability to circulate multiple times before recombining with their opposite, as represented in Fig. 6b. This results in an internal gain and an EQE larger than 1. When materials are separated by electrodes and exposed to light, the former is interested in how their overall conductivity changes. Aside from this, the charge transfer carrier efficiency between the Bi_2S_3 and PANI plays a significant role in quick photoresponse. As a result of the direct Bi–C bond in the $\text{Bi}_2\text{S}_3/\text{PANI}$ nanohybrid, an immediate electron transfer occurs at the Bi_2S_3 and PANI interface, enhancing photodetection activity as represented in Fig. 6c.

In essence, an MSM structure is two Schottky barriers connected back-to-back. Figure 6d shows the MSM photodetector in the thermal equilibrium condition with built-in voltages V_1 and V_2 , and the Schottky barrier heights for electrons at contacts 1 and 2 are Φ_1 and Φ_2 , respectively. Since $\Phi_1 = \Phi_2$ under ideal circumstances (identical metals with equal contact areas), such MSM structure is known as symmetric. The electrons are at their lowest energy states at $T=0$ K. Because some electrons have hopped to higher energy levels with rising thermal energy, there is a non-zero probability that electrons will inhabit certain energy states above E_F , and some energy states below E_F will be unoccupied above absolute temperature. Figure 6e shows the MSM structure with applied bias in a dark environment, with contact 1 having reversed bias and contact 2 having forward bias. Biasing causes the depletion width of contact 1 to widen and contact 2 to narrow. In this instance, electrons move through thermionic emission from contact 1 to contact 2 with potential barrier Φ_1 . As a result, the amount of the resulting reverse bias dark current at contact 1 is relatively small. A comparable dark current is seen at contact 2 when the polarity of both connections is reversed. In the channel layer, e–h pairs are produced under optical light. A current corresponding to the incident photon flux is made due to the separation of these photogenerated carriers by the inherent or applied electric field. As seen in Fig. 6f, the holes in the VB become stimulated as the electrons move into the CB. Additionally, the photocurrent in the device is facilitated by electrons and holes drifting in the direction of contacts

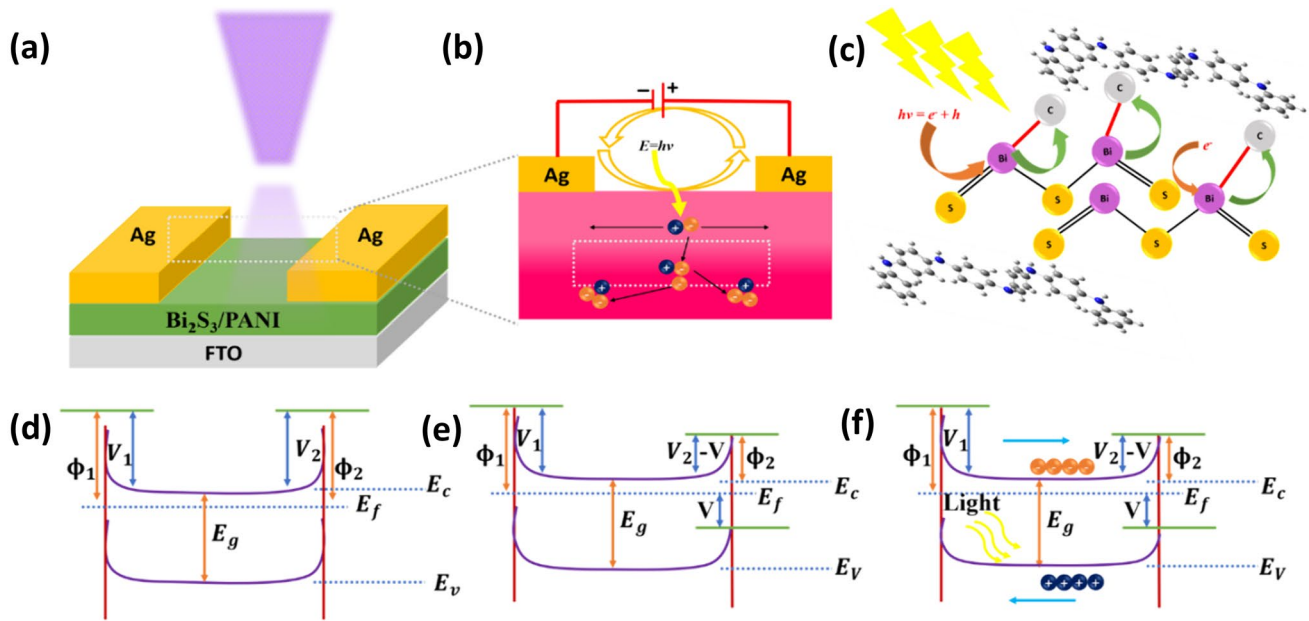


Fig. 6 **a** The schematic illustration of the MSM photodetector device, **b** a diagrammatic photomultiplication phenomenon occurs in the photodetector device, **c** a schematic demonstration model of the Bi-C bonding in Bi₂S₃/PANI nanohybrid provides high charge carriers

transfer activity in the photodetection; energy band diagram of MSM photodetector under **d** thermal equilibrium condition, **e** applied bias *V* in the dark condition, and **f** applied bias *V* upon illumination of light

2 and 1, respectively. The high conductivity is due to the conjugation of the conducting polymer and Bi₂S₃ with the PANI-based nanohybrid, which enhanced the overall conductivity of the photodetector device.

Mott-Schottky (M-S) investigations have been carried out to elucidate further the reason for the better photodetection performance of the as-fabricated Bi₂S₃ and Bi₂S₃/PANI photodetector device in terms of charge carrier density and flat band potential. The donor density (*N_D*), as well as the flat band potential (*V_{FB}*) for the fabricated photodetector devices, can be determined by the following M-S relation for n-type semiconductors as given in Eq. (2):

$$\frac{1}{C_{sc}^2} = \frac{2}{\epsilon_0 \epsilon_r N_D} \left[V - V_{FB} - \frac{K_B T}{e} \right] \tag{2}$$

where *C_{SC}* is the space charge capacitance, ϵ_r refers to the semiconductor’s dielectric constant (ϵ_r for Bi₂S₃ is 0.5 at 1 kHz), ϵ_0 is the permittivity of vacuum ($8.85 \times 10^{-12} \text{ Fm}^{-1}$), *e* is the electron charge ($1.6 \times 10^{-19} \text{ C}$), *K_B* is the Boltzmann constant, *T* is the absolute temperature, and *V* is the applied potential. Typically, the M-S relationship is obtained by considering two capacitances in series combination at the interface of electrode/electrolyte: (i) space charge capacitance (*C_{SC}*) and (ii) Helmholtz layer capacitance (*C_H*); the semiconductor capacitance varies with the extent of band bending while the capacitance of the Helmholtz layer remains constant; thus, $C_{SC} \ll C_H$, such that $C_{SC} \approx C_{\text{interface}}$. The

positive and negative slopes of the M-S plot indicate the n- and p-type conductivity of the semiconductor, respectively [65].

Bi₂S₃ and Bi₂S₃/PANI as-fabricated photodetector devices exhibit a linear region with a positive slope in the M-S plot, indicating the n-type properties of Bi₂S₃ material with electrons as the predominant carriers. Interestingly, extrapolating the linear component of the M-S curve to the *x*-axis intercept allows one to determine the values of *V_{FB}* for photodetector devices. It is observed that when PANI is incorporated with Bi₂S₃ nanoflowers, the *V_{FB}* value shifts from 0.33 V for Bi₂S₃ to 0.05 V for the Bi₂S₃/PANI photodetector device as shown in Fig. S3. This decrease in *V_{FB}* confirms enhanced bending at the electrode interface, favoring higher separation and quicker transfer of photogenerated charge carriers. By changing the value of the slope of the linear sections of the M-S plots in the following formula, the values of the donor density (*N_D*) are estimated by Eq. (3):

$$N_D = \frac{2}{e \epsilon_0 \epsilon_r} \left[\frac{d(1/C^2)}{dV} \right]^{-1} \tag{3}$$

The value of *N_D* is estimated as $0.85 \times 10^{21} \text{ cm}^{-3}$ for Bi₂S₃ and $5.64 \times 10^{21} \text{ cm}^{-3}$ Bi₂S₃/PANI photodetector device. The Bi₂S₃/PANI photodetector device has demonstrated higher *N_D* value of $5.64 \times 10^{21} \text{ cm}^{-3}$ which suggests improved charge transportation and suppressed recombination rate of the photogenerated charge carriers caused by

established type II heterojunction resulting in enhanced electrical conductance [67–73]. It is worth noting that the increment in the N_D of different semiconductors after heterojunction formation with PANI is also reported in the literature [74–77].

We know that photocurrent as a function of time ($I-t$ curve) can be used to examine its capacity to respond quickly and its stability, which are two crucial properties of photodetector devices. $I-T$ measurements of the $\text{Bi}_2\text{S}_3/\text{PANI}$ photodetector device were recorded for various on/off states for UV and visible light under different illumination intensities at the constant bias of 1 V, as shown in Fig. 7a and b. The photocurrent quickly reaches a maximum value and then swiftly returns to its initial stage with the light on/off. The photocurrent switch with the on–off states of light illumination can be performed numerous times without noticeably degrading, showing the photodetector’s outstanding reaction capabilities and photostability in its as-fabricated form. At the potential drift of 1 V, on increasing the intensity of the light current rises due to the production of more photogenerated electron and hole pairs, which results in a fast response. However, the $\text{Bi}_2\text{S}_3/\text{PANI}$ hybrid system is accurate for visible light as per the band gap energy in the broad EM spectrum. At the constant illumination intensity of $50 \mu\text{Wcm}^{-2}$, the $I-t$ curves were recorded at various potential drifts for the UV and visible regions, as shown in Fig. 7c and d. From this, it can be seen that the photoconductivity rises with the potential bias due to the electric field between the electrodes.

A certain level of bulk and surface defects in semiconductors can lead to trap states with energies within the band gap, dramatically altering the actual shape of the $I-V$ characteristics. The $I-V$ characteristics demonstrate that the curve follows $I=kV^2$ when the concentration of injected carriers is greater than that of background charge carriers, where k is dictated by the trap states present in the material [54, 59]. The current obeys the rule $I \propto V^n$ as the voltage is increased up to and beyond the turning voltage. At lower voltages, trapped electrons and holes that are only partially filled can readily drift away from the corresponding injection electrode; the accumulating space charge does not impact carriers. All trap states are filled at high voltages, considerably reducing the ability to inject carriers [78].

Additionally, the area next to the electrode prevents carrier injection. These $I-V$ characteristics with trap states adhere to the Mott-Gurney law [79]. When illuminated at a low voltage, most carriers (electrons) have sufficient mobility and a shorter transit than the carrier’s lifespan. Electrons are swept out of the PD quickly, but surplus holes remain because the minority carrier (hole) has a slow drift speed and a transit time longer than the carrier’s lifespan. The $I-V$ characteristics of the nanohybrid device for the UV region and visible region with varying illumination intensities ($50\text{--}375 \mu\text{Wcm}^{-2}$) as shown in Fig. 8a and b. When exposed to light, an enhanced light-induced current or photoconductivity is detected in the $I-V$ curves for the $\text{Bi}_2\text{S}_3/\text{PANI}$ photodetector. Such an increase in photoconductivity is more readily gained in the visible than in the UV region.

Fig. 7 **a** $I-t$ curves in the UV region and **b** $I-t$ curves in the visible region at the constant bias of 1 V, **c** $I-t$ curves in the UV region, and **d** $I-t$ curves in the visible region at constant illumination of $50 \mu\text{Wcm}^{-2}$

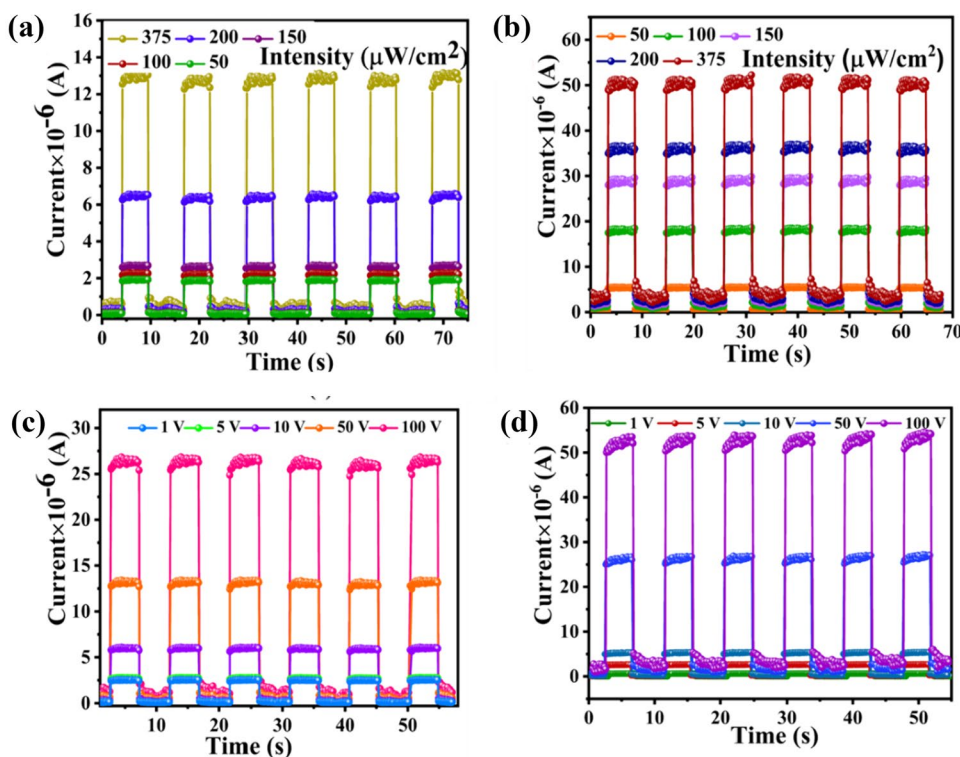
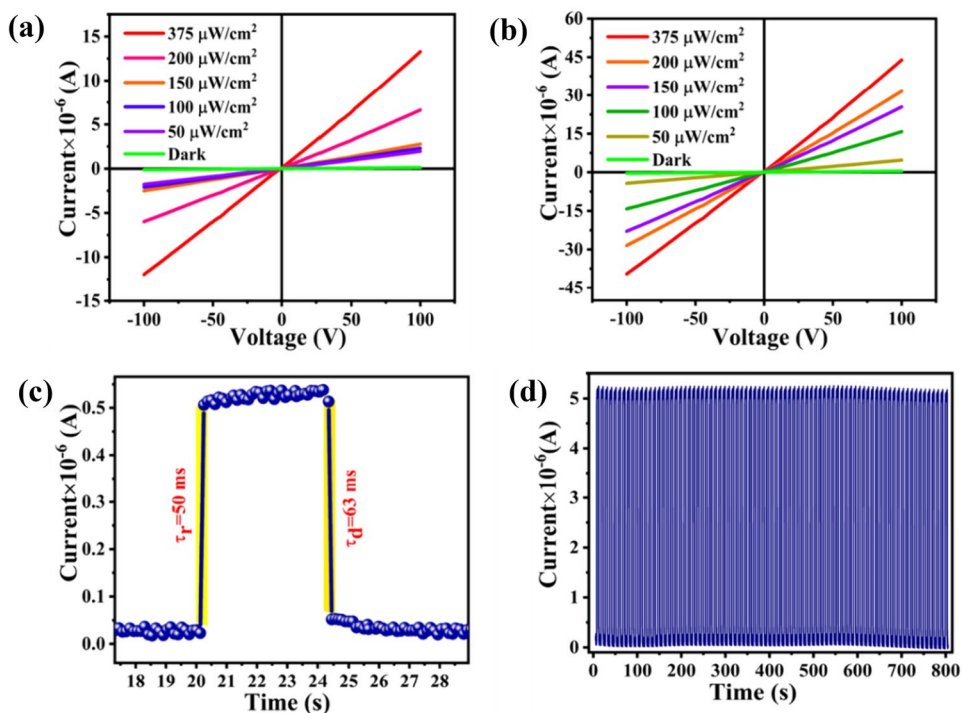


Fig. 8 **a** I - V characteristics in the UV region, **b** I - V curves in the visible region, **c** rise and decay times for one on/off state, and **d** stability of the device at the bias voltage of 10 V with $50 \mu\text{Wcm}^{-2}$



This demonstrates that a stronger photoresponse is detected in the visible region, consistent with the previously reported results [3]. The MSM photodetector device of $\text{Bi}_2\text{S}_3/\text{PANI}$ shows a good Ohmic nature in UV and visible regions. It is possible to describe devices with I - V curves restricted to the first and third quadrants of the I - V plane and pass through the origin as passive components that draw electricity from the source. Traditional current causes the charges to lose potential energy, which can be converted into heat or other forms of energy, as it flows through this Ag/nanohybrid/Ag device from the positive voltage terminal to the negative voltage terminal in the direction of the electric field [40]. As can be seen from Fig. 8a and b, the dark current is about $0.003 \mu\text{A}$, and the currents under UV illumination and visible illumination were found to be $0.58 \mu\text{A}$ and $2.58 \mu\text{A}$ at the potential drift of 1 V with the illumination intensity of $50 \mu\text{Wcm}^{-2}$.

When exploring photoconductivity, we can learn critical details about the material by examining how photocurrent varies with light intensity, applied field, illumination energy, temperature, and other characteristics. The charge trapping and recombination process within the material is given some insight by the fluctuation of photocurrent with light intensity response. The nature of the distribution of traps and recombination centers can be ascertained by observing the increase and decline of photocurrent with time response. The rise and fall time are defined as the time required for the photocurrent (I_p) transition from 0 to 100%, which is an essential parameter of the photodetector device. The carrier generation and recombination can be understood based on the rise and decay times.

The rise and decay times are analyzed by the exponential fitting of time-dependent photocurrent data as given by relations (4) and (5), respectively.

$$I(t) = I_{\text{dark}}(e^{-t/\tau_r}) \quad (4)$$

$$I(t) = I_{\text{dark}}(1 - e^{-t/\tau_d}) \quad (5)$$

One cycle of the I - t curves was taken to measure the device's response time, and the rise/decay time was found to be 50/63 ms, as shown in Fig. 8c. As the Bi-C bond provides a fast electron transfer pathway, the interaction of the conjugated polymer with the Bi_2S_3 nanorods enhanced the photodetection characteristics of the $\text{Bi}_2\text{S}_3/\text{PANI}$ nanohybrid. The stability of the $\text{Bi}_2\text{S}_3/\text{PANI}$ photodetector device up to 800 s at the minimum intensity of the optical signal is represented in Fig. 8d. Also, the stability of the $\text{Bi}_2\text{S}_3/\text{PANI}$ nanohybrid photodetector device over 3000 s at the interval of 50 s is presented in Fig. S4. The responsivity (R) of the photodetector is defined as the photocurrent generated per unit area and unit incident light as expressed by Eq. (6):

$$\text{Responsivity}, R = \frac{I_p - I_d}{AP_{in}} \text{ A W}^{-1} \quad (6)$$

Responsivities of $\text{Bi}_2\text{S}_3/\text{PANI}$ photodetector device were found to be 270 mA W^{-1} and 1270 mA W^{-1} with the illumination intensity of $50 \mu\text{Wcm}^{-2}$ under UV and visible regions, respectively, at the potential drift of 1 V as shown in Fig. 9a and b. This value is more than the lead-free $\text{CsCu}_2\text{I}_3/\text{GaN}$

heterostructure photodetector [80]. The maximum responsivities were $26,760 \text{ mA W}^{-1}$ and $13,250 \text{ mA W}^{-1}$ at 100 V with $50 \mu\text{W cm}^{-2}$ due to the photocurrent increasing linearly with the potential drift. The responsivity of the $\text{Bi}_2\text{S}_3/\text{PANI}$ photodetector device was determined for UV and the visible regions on increasing illumination intensity, as depicted in Tables S1 and S2. This high level of responsivity can be attributed to the photomultiplication process, in which photocarriers pass through the circuits numerous times before recombination. Only PD devices with a photoconductor-based architecture may accomplish this photomultiplication operation. Photoresponsivity rises as the quantity of photons incident on the specific device's active area increases with light intensity.

Additionally, at the constant illumination intensity of $50 \mu\text{W cm}^{-2}$, the potential bias is raised up to 100 V. As the number of photons rises, the photoresponsivity also increases, as shown in the graph (Fig. 10a, b) for visible and UV regions. The responsivity, which has a linear relationship with the external quantum efficiency (EQE), measures the strength of the photogenerated electric signal under a specific illumination intensity. The quantity of e-h pairs generated by each incident photon is known as the EQE given by Eq. (7):

$$\text{External quantum efficiency, EQE} = \frac{R \times h \times c}{e \times \lambda} \times 100\% \quad (7)$$

Generally, the EQE for p-n junction-type devices is less than 100%. However, because of the photomultiplication process in MSM photodetector devices, the EQE was more than 100%, as we have seen that the EQE of the $\text{Bi}_2\text{S}_3/\text{PANI}$ MSM photodetector device are estimated to be 102% and 431% at the potential drift of 1 V with the illumination intensity of $50 \mu\text{W cm}^{-2}$ for UV and visible regions respectively as shown in Fig. 9a and b. The EQE rises as the light's photon density increases, as shown in Tables S1 and S2. Also, the highest EQE for UV and visible regions were found to be 9073% and 4493%, respectively, as the potential drift is directly proportional to the EQE. The higher EQE allows us to detect the lower photon intensity so that these flexible devices can be implemented in research areas requiring lower irradiance detection. The highest EQE was reached in the $\text{Bi}_2\text{S}_3/\text{PANI}$ MSM photodetector because generating a more significant number of electrons due to light illumination increased the photocurrent, and the responsivity corresponding to EQE also increased.

All the qualitative parameters of the $\text{Bi}_2\text{S}_3/\text{PANI}$ photodetector device at different illumination intensities of the optical signal under UV and visible spectra at a constant potential drift of 1 V are tabulated in Tables S1 and S2,

respectively. The capacity of the device to detect weak optical signals is also an essential parameter of the photodetector device. The noise sources in the photodetector are mainly due to the contributions from dark current and thermal fluctuations. The detectivity of the device can be determined by Eq. (8):

$$\text{Detectivity, } D = \sqrt{\frac{A}{2eI_d}} R \text{ Jones or cm } \sqrt{\text{Hz W}^{-1}} \quad (8)$$

The detectivity of $\text{Bi}_2\text{S}_3/\text{PANI}$ photodetector device were found to be 5.91×10^{11} Jones and 2.49×10^{12} Jones at 1 V with an illumination intensity of $\mu\text{W cm}^{-2}$ for UV and visible regions, respectively. The device's highest detectivities were 5.24×10^{13} Jones and 2.59×10^{13} Jones for UV and the visible regions at 100 V of applied voltage with a minimum illumination intensity of $50 \mu\text{W cm}^{-2}$, as shown in Fig. 10c and d. And on increasing the illumination intensity from $50 \mu\text{W cm}^{-2}$, we found the detectivity of the order of 10^{13} Jones. The bilayer-based hybrid photodetector of $\text{TiO}_2/\text{GQDs-CsPbBr}_3$ composite has responsivity 7.11 AW^{-1} and detectivity 3.32×10^{12} Jones at 10 V as previously reported [81]. The superior alignment of the anatase TiO_2 , GQDs, and CsPbBr_3 allowed the $\text{TiO}_2/\text{GQDs-CsPbBr}_3$ bilayer heterojunction to decrease recombination and boost photon absorption rate, which in turn led to the improved performance of the hybrid photodynamic filter. Another critical parameter of the photodetector devices is the noise equivalent power (NEP), defined as a certain level of noise in which dark current is generated as given in relation (9):

$$\text{Noise equivalent power, NEP} = \frac{I_d}{R} \text{ W} \quad (9)$$

NEP, which indicates the limit detection capability for photodetectors and describes the detection performance of the photodetectors to the weakest light, is the input signal power necessary to generate a signal equal to the noise output of the detector. The capacity for detecting weak light improves with decreasing NEP values. When the photocurrent is slightly higher than the noise current or equal to it, the photodetectors can detect the lowest light energy. NEP of the $\text{Bi}_2\text{S}_3/\text{PANI}$ photodetector device were found to be $1.08 \times 10^{-7} \text{ W}$ and $2.56 \times 10^{-8} \text{ W}$ for UV and visible regions, respectively, at 1 V with an illumination intensity of $50 \mu\text{W cm}^{-2}$ as shown in Fig. 10c and d. The minimum value of NEP found in the order of 10^{-9} W which is the lowest value, suggests that the nanohybrid material is perfect for low-intensity photon signals. You may evaluate the quality of the photodetector by looking at the ratios of signal to noise and photocurrent to dark current [82]. The linear

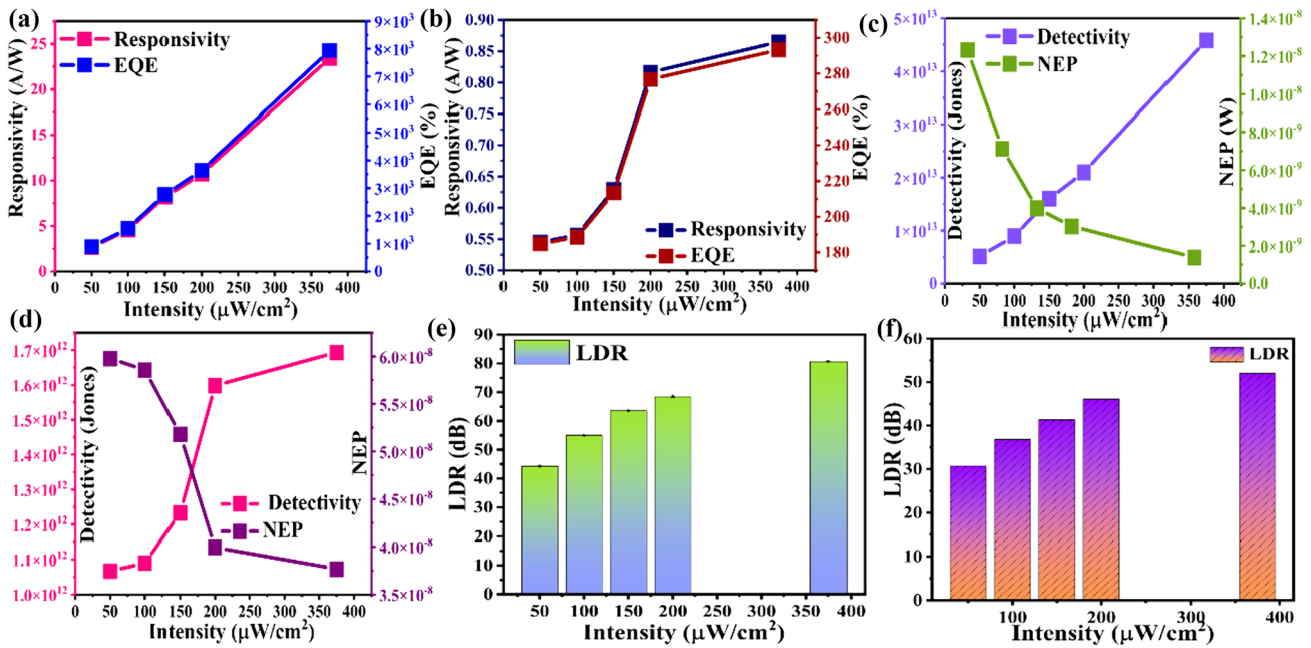


Fig. 9 **a** Graph of responsivity and EQE in the UV region, **b** graph of responsivity and EQE in the visible region, **c** detectivity and NEP in UV region, **d** detectivity and NEP in the visible region, **e** LDR in

the UV region, **f** LDR in the visible region under various illumination intensity at the constant potential bias of 1 V

dynamic range (LDR) of a device is defined as the linearity of the device up to the point at which the response of the device is linear and evaluated by using relation (10):

$$\text{Linear dynamic range, LDR} = 20\log\left(\frac{I_p}{I_d}\right) \text{ dB} \quad (10)$$

LDR of the photodetector device were found to be 25.83 dB and 37.96 dB at 1 V with an illumination intensity of $50 \mu\text{Wcm}^{-2}$ for UV and visible regions, respectively, as shown in Fig. 9e and f. The higher values of the LDR are 64.31 dB and 58.21 dB at 100 V, with the lowest illumination intensity as shown in Fig. 10e and f.

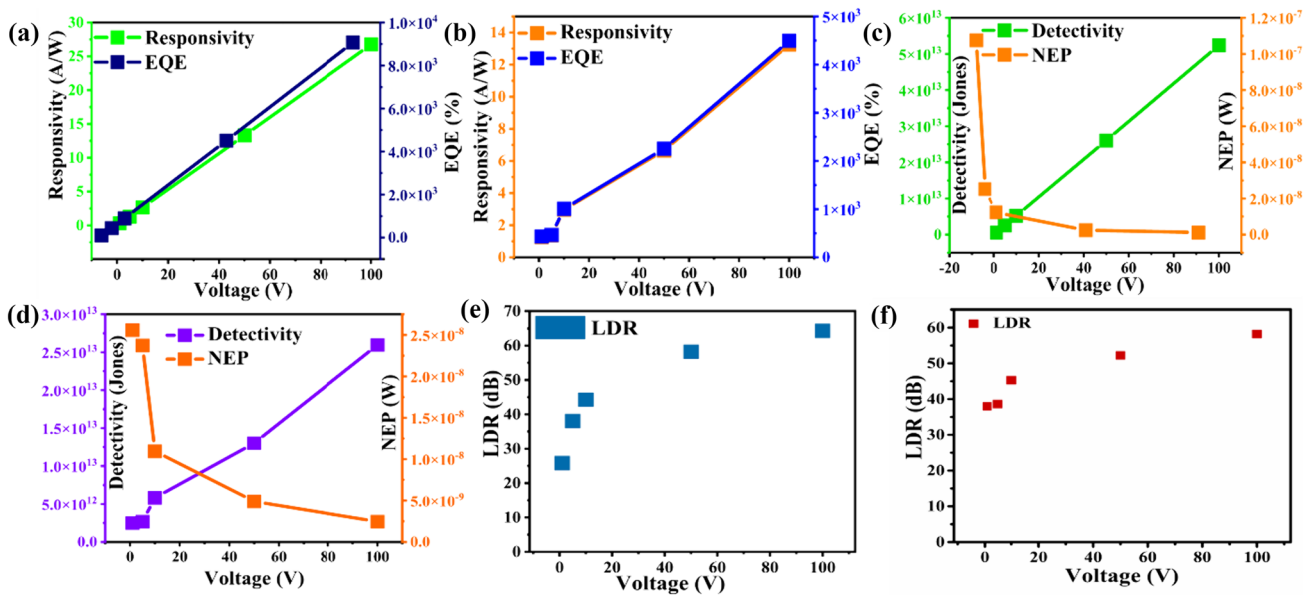


Fig. 10 **a** Graph of responsivity and EQE in the UV region, **b** graph of responsivity and EQE in the visible region, **c** detectivity and NEP in UV region, **d** detectivity and NEP in the visible region, **e** LDR in

the UV region, **f** LDR in the visible region under various potential bias condition at constant illumination of $50 \mu\text{Wcm}^{-2}$

As shown, the photocurrent is saturated in both the UV and visible spectrums of the $\text{Bi}_2\text{S}_3/\text{PANI}$ MSM photodetector after $100 \mu\text{Wcm}^{-2}$, according to our estimations, when the illumination intensity is increased at a constantly applied drift of 1 V. However, as the electric field between the electrodes increases with applied potential, the photocurrent rises even at the lowest illumination of the optical signals. All the figures of merits are tabulated in Tables S3 and S4 at the constant illumination with varying potential drift. Responsivity, EQE, and detectivity are proportional to the photocurrent of the photodetector device since they correspond to it. H. Algadi et al. reported MoS_2/NH_2 GQDs/ CsPbBr_3 triple junction-based hybrid photodetector with responsivity 9.39 AW^{-1} , detectivity 3.32×10^{12} Jones, and EQE 791% at 10 V [23] is consistent with $\text{Bi}_2\text{S}_3/\text{PANI}$ based photodetector device. The exceptional alignment of the MoS_2 , NH_2 GQDs, and CsPbBr_3 allowed the triple junction to decrease recombination and increase the photon-absorption rate, which improved the hybrid PD's performance. The $\text{Bi}_2\text{S}_3/\text{PANI}$ nanohybrid shows better responsivity 23.41 AW^{-1} , EQE 7939%, and detectivity 4.59×10^{12} Jones at the bias voltage of 10 V with the light intensity of $375 \mu\text{Wcm}^{-2}$. The qualitative parameters of the nanohybrid device are increased with the optical power, and the PANI provides conjugation to the Bi_2S_3 materials due to the coupling of the organic and inorganic components.

Also, we have studied the compositional study of the $\text{Bi}_2\text{S}_3/\text{PANI}$ nanohybrid with varying the aniline monomer with a molarity of 1M, 0.8 M and 0.6 M. The I - V characteristics of 0.8 M and 0.6 M hybrid samples are represented in Fig. S5. The performance of the device's attributes of the $\text{Bi}_2\text{S}_3/\text{PANI}$ nanohybrid photodetector device when subjected to a bias potential of 1 V and an illumination intensity of $50 \mu\text{Wcm}^{-2}$. At the highest polyaniline concentration of 1 M, the device exhibits a remarkable UV responsivity of $1078.95 \text{ mA W}^{-1}$, showcasing its efficiency in converting UV light into electrical signals. Moreover, its exceptionally high detectivity of 2.11×10^{12} Jones in the UV region suggests its capability to detect even faint UV light signals with minimal noise interference. Transitioning to the visible region, the device maintains a respectable responsivity of 302.90 mA W^{-1} at the 1 M concentration, albeit lower than that of the UV region. This signifies its ability to convert visible light into electrical signals, albeit with a slightly reduced efficiency compared to UV light. The corresponding detectivity of 5.93×10^{11} Jones underscores its effectiveness in detecting weak light signals. The highest responsivity and detectivity were found at the 1 M concentration of the monomer aniline, as depicted in Table S5. However, as the polyaniline concentration decreases to 0.8 M, both responsivity and detectivity values diminish significantly in UV and visible regions. The UV responsivity drops to 26.13 mA W^{-1} , reducing the ability to convert UV light into electric signals.

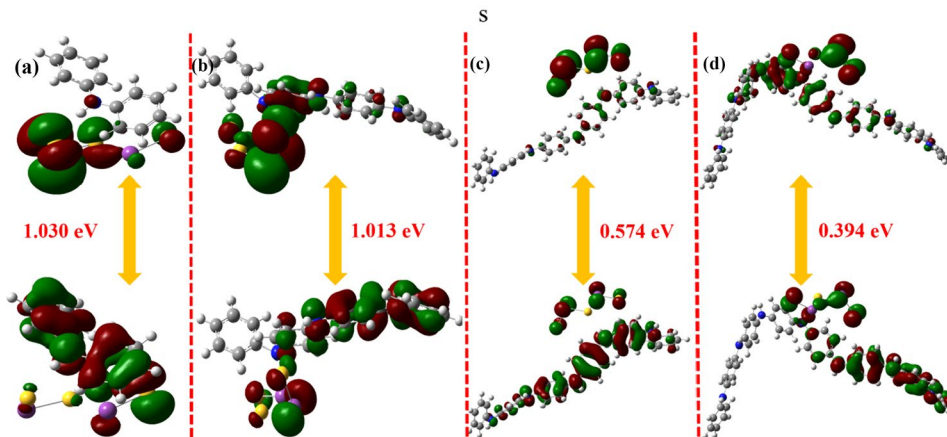
In contrast, the UV detectivity decreases the ability to convert UV light into electric signals, while the UV detectivity decreases to 7.43×10^{10} Jones, suggesting a reduced capacity to detect weak UV light signals while maintaining low noise levels. Similarly, in the visible region, the responsivity decreases to 15.34 mA W^{-1} , and the detectivity decreases to 1.06×10^{11} Jones. The corresponding responsivity and detectivity of the samples are plotted against the molar concentration of the aniline monomer, as given in Fig. S6. At the lowest PANI concentration of 0.6 M, both responsivity and detectivity values experience further declines. The UV responsivity is reported as 20.42 mA W^{-1} , indicating a further reduction in the device's ability to convert UV light into electrical signals. The corresponding UV detectivity decreases to 1.12×10^{11} Jones, indicating a lower sensitivity to weak signals. In the visible region, the responsivity decreases to 8.72 mA W^{-1} , and the detectivity decreases to 4.77×10^{10} Jones, highlighting a reduced ability to convert and detect visible light signals.

3.5 Charge carrier dynamics analysis utilizing density functional theory (DFT)

The transfer of charge carriers and the transmission of excitation energy are the two critical processes for a detailed understanding of optoelectronic devices. The process of electron transfer occurs when the occupancy of two molecular orbitals interacts. Light harvesting and photocurrent analysis use the singlet and triplet excitation energy transfer [64]. To completely understand these systems, it is essential to characterize the rates of the processes using the fewest possible empirically determined parameters. In such a molecular model, the analysis was carried out by employing a varied chain length of the PANI with Bi_2S_3 . The density functional theory (DFT) of the $\text{Bi}_2\text{S}_3/\text{PANI}$ molecules was designed by using Gauss View 5.0, and their structures were optimized using Gaussian 09 and the B3LYP* basis set. Using this computational method, we have examined the four distinct species as tabulated in Table 2. In the Bi_2S_3 , HOMO and LUMO energies are -6.62 eV and -4.29 eV , respectively. Two units of PANI and one unit of Bi_2S_3 combine to generate the species $2\text{PANI-Bi}_2\text{S}_3$. The energies of the HOMO and the LUMO are -4.73 eV and -3.70 eV , respectively. Four units of PANI and one unit of Bi_2S_3 combine to generate the species $4\text{PANI-Bi}_2\text{S}_3$. The HOMO and LUMO energies are 3.80 eV and -2.78 eV . Also, the HOMO and LUMO energies of $6\text{PANI-Bi}_2\text{S}_3$ are -2.93 eV and -2.35 eV , respectively. The HOMO energy is -4.32 eV while the LUMO energy is -3.93 eV , according to $8\text{PANI-Bi}_2\text{S}_3$. In a molecule, the HOMO energy denotes the highest energy level occupied by electrons, whereas the LUMO energy denotes the lowest unoccupied energy level [83, 84]. The HOMO-LUMO gap, which measures the energy difference between the HOMO

Table 2 DFT-based electronic parameters of all investigated species

Species	HOMO (eV)	LUMO (eV)	Band gap (eV)
Bi ₂ S ₃	-6.62	-4.29	2.32
2PANI-Bi ₂ S ₃	-4.73	-3.70	1.03
4PANI-Bi ₂ S ₃	-3.80	-2.78	1.01
6PANI-Bi ₂ S ₃	-2.93	-2.35	0.57
8PANI-Bi ₂ S ₃	-4.32	-3.93	0.394

Fig. 11 HOMO–LUMO band gap energy of species **a** 2PANI-Bi₂S₃, **b** 4PANI-Bi₂S₃, **c** 6PANI-Bi₂S₃, and **d** 8PANI-Bi₂S₃

and LUMO levels, is a sign of the electronic characteristics of the molecule, including its stability, conductivity, and capacity to provide or take electrons.

The HOMO and LUMO energies of these species can be used to gain further knowledge about the electronic structures of these species and possible interactions with other molecules. HOMO and LUMO energies tend to drop as the number of PANI units increases, suggesting that PANI may affect the electrical properties of nanohybrid materials. Interactions between the PANI and Bi₂S₃ components in the hybrid materials cause the observed trend in the HOMO and LUMO energies for the species. It is well known that the delocalized π -electron system in PANI can extend along the polymer chain. The conjugated π -electron system of PANI can interact with the electronic structure of Bi₂S₃ when PANI units and Bi₂S₃ are coupled [85]. This interaction might change the HOMO and LUMO energies because it might reshuffle the electron density. The presence of PANI units can facilitate charge transfer between PANI and Bi₂S₃. PANI units increase the number of electron-donating groups in the composite material, which may affect the ability of Bi₂S₃ to receive electrons. This interaction could lead to a redistribution of the electron density, changing the HOMO and LUMO energies. The energy levels of the HOMO and LUMO orbitals may be impacted by this charge transfer, resulting in a drop in their energies [86]. PANI units can induce alterations in the structure of hybrid materials. The positioning and orientation of PANI units can affect the

electronic composition and energy levels of the material. The conformational changes become more critical as the PANI unit count rises, changing the HOMO and LUMO energies [87].

The band gap for Bi₂S₃ is relatively high at 2.32 eV compared to PANI-doped nanohybrids. This shows that the passage of electrons in Bi₂S₃ from the VB to the CB takes a lot of energy. The band gap rapidly narrows when PANI is imple-

mented, and the doping level rises, as depicted in Fig. 11. The band gap for 2PANI-Bi₂S₃ falls to 1.03 eV, showing that the substance is transitioning from an insulator to a semiconductor. With 4PANI-Bi₂S₃, the band gap narrows until it reaches 1.01 eV. When we get to 6PANI-Bi₂S₃, the band gap is 0.57 eV. The substance is expected to expand more conductive and exhibit semiconductor characteristics by virtue of this value. Finally, the band gap of 8PANI-Bi₂S₃ further decreases to 0.39 eV, demonstrating that it is rapidly approaching conductor-like features. The band gap gradually narrows as the degree of PANI doping in the Bi₂S₃ material rises. This pattern shows a change from an insulating substance (Bi₂S₃) to a behavior more like a semiconductor (2PANI-Bi₂S₃, 4PANI-Bi₂S₃) and finally to a more conductive substance (6PANI-Bi₂S₃, 8PANI-Bi₂S₃).

4 Conclusions

We successfully synthesized hierarchical nanoflowers of Bi₂S₃ nanorods and Bi₂S₃/PANI nanohybrid. Further, Bi₂S₃/PANI nanohybrid was used to fabricate the MSM photodetector device on the FTO substrate utilizing the solution-processed method. Then, the prepared nanohybrid was used for the photodetection measurement in the UV and visible range. Additionally, the Bi-C bonding in the Bi₂S₃/PANI nanohybrid facilitates the charge carriers transfer from Bi₂S₃

to the conjugated polymer, leading to a higher response from the photodetection. The synergetic effect of the Bi_2S_3 and PANI in the $\text{Bi}_2\text{S}_3/\text{PANI}$ nanohybrid enhanced the overall performance of the photodetector device. The $\text{Bi}_2\text{S}_3/\text{PANI}$ MSM photodetector device shows the maximum responsivities were $26,760 \text{ mA W}^{-1}$ and $13,250 \text{ mA W}^{-1}$ at 100 V with $50 \mu\text{W cm}^{-2}$. The device's highest detectivities were 5.24×10^{13} Jones and 2.60×10^{13} Jones for UV and visible regions at 100 V of applied voltage with a minimum illumination intensity of $50 \mu\text{W cm}^{-2}$. Also, the highest EQE were found to be 9073% and 4493% for UV and visible regions. Additionally, we found that the material shows high NEP and LDR values, which is most important for weak optical detection. At a constant potential drift, on increasing the illumination intensity of the light after, we found that the nanohybrid materials possess excellent properties in the broad range of the EM spectrum.

5 Supporting information

Scanning electron microscopy of the Bi_2S_3 and the photodetector parameters of $\text{Bi}_2\text{S}_3/\text{PANI}$ represented in the UV and visible regions. Compositional study of the nanohybrid samples and Mott-Schottky graphs, stability of the photodetector device over 3000 s and DFT parameters of the four species of the nanohybrid samples and s/b under author contribution.

Supplementary Information The online version contains supplementary material available at <https://doi.org/10.1007/s42114-024-00878-7>.

Acknowledgements Anshika Singh is thankful to the University grants commission (UGC) Delhi, India, for the financial support.

Author contribution Anshika Singh: writing—original draft, conceptualization, methodology, validation, investigation, resources. Arpit Verma: conceptualization, visualization, and discussions. Bal Chandra Yadav: visualization and discussions. Pratima Chauhan: supervision, review, and editing. During the revision also, all the authors reviewed the entire manuscript.

Declarations

Competing interests The authors declare no competing interests.

References

- Zhu J, Yang K, Zhu J, Ma G, Zhu X, Zhou S et al (2003) The microstructure studies of bismuth sulfide nanorods prepared by sonochemical method. *Opt Mater* 23:89–92
- Ding T, Dai J, Xu J, Wang J, Tian W, Huo K et al (2015) 3D hierarchical Bi_2S_3 nanostructures by polyvinylpyrrolidone (PVP) and chloride ion-assisted synthesis and their photodetecting properties. *Nanoscale Res Lett* 10:1–8
- Huo N, Figueroba A, Yang Y, Christodoulou S, Stavrinadis A, Magén C et al (2019) Engineering vacancies in Bi_2S_3 yielding sub-bandgap photoresponse and highly sensitive short-wave infrared photodetectors. *Adv Opt Mater* 7:1900258
- Salavati-Niasari M, Behfard Z, Amiri O (2014) Synthesis of bismuth sulfide nanostructures by using bismuth (III) monosalicylate precursor and fabrication of bismuth sulfide based p–n junction solar cells. *Asia-Pac J Chem Eng* 9:16–23
- Shahbazi M-A, Faghfour L, Ferreira MP, Figueiredo P, Maleki H, Sefat F et al (2020) The versatile biomedical applications of bismuth-based nanoparticles and composites: therapeutic, diagnostic, biosensing, and regenerative properties. *Chem Soc Rev* 49:1253–1321
- Supekar AT, Bhujbal PK, Salunke SA, Rathod SM, Patole SP, Pathan HM (2023) Bismuth sulfide and antimony sulfide-based solar cells: a review. *ES Energy Environ* 19:848
- Yu Y, Jin C, Wang R, Chen Q, Peng L-M (2005) High-quality ultralong Bi_2S_3 nanowires: structure, growth, and properties. *J Phys Chem B* 109:18772–18776
- Zhang H, Ji Y, Ma X, Xu J, Yang D (2003) Long Bi_2S_3 nanowires prepared by a simple hydrothermal method. *Nanotechnology* 14:974
- Lu J, Han Q, Yang X, Lu L, Wang X (2007) Microwave-assisted synthesis and characterization of 3D flower-like Bi_2S_3 superstructures. *Mater Lett* 61:2883–2886
- Xiang W, Yang Y, Yang J, Yuan H, An J, Wei J et al (2014) Surfactant and thioacetamide-assisted reflux synthesis of Bi_2S_3 nanowires. *J Mater Res* 29:2272–2287
- Lu Q, Gao F, Komarneni S (2004) Biomolecule-assisted synthesis of highly ordered snowflake-like structures of bismuth sulfide nanorods. *J Am Chem Soc* 126:54–55
- Panigrahi PK (2013) Pathak A. The growth of bismuth sulfide nanorods from spherical-shaped amorphous precursor particles under hydrothermal condition. *J Nanopart* 37:457–69
- Neog A, Biswas R (2021) WS_2 nanosheets as a potential candidate towards sensing heavy metal ions: a new dimension of 2D materials. *Mater Res Bull* 144:111471
- Ahmed AA, Devarajan M, Afzal N (2017) Fabrication and characterization of high performance MSM UV photodetector based on NiO film. *Sens Actuators, A* 262:78–86
- Badhulika S (2022) A flexible, rapid response, hybrid inorganic-organic SnSe_2 -PEDOT: PSS bulk heterojunction based high-performance broadband photodetector
- Yang X, Bao D, Zhang Y, Li B (2016) Single crossed heterojunction assembled with quantum-dot-embedded polyaniline nanowires. *ACS Photonics* 3:1256–1264
- Zang L (2015) Interfacial donor–acceptor engineering of nanofiber materials to achieve photoconductivity and applications. *Acc Chem Res* 48:2705–2714
- Chen H, Liu K, Hu L, Al-Ghamdi AA, Fang X (2015) New concept ultraviolet photodetectors. *Mater Today* 18:493–502
- Tian W, Lu H, Li L (2015) Nanoscale ultraviolet photodetectors based on one-dimensional metal oxide nanostructures. *Nano Res* 8:382–405
- Dong R, Bi C, Dong Q, Guo F, Yuan Y, Fang Y et al (2014) An ultraviolet-to-NIR broad spectral nanocomposite photodetector with gain. *Adv Opt Mater* 2:549–554
- Wu S-h, Li W-l, Chu B, Su Z-s, Zhang F, Lee CS (2011) High performance small molecule photodetector with broad spectral response range from 200 to 900 nm. *Appl Phys Lett* 99:134
- O'Brien GA, Quinn AJ, Tanner DA, Redmond G (2006) A single polymer nanowire photodetector. *Adv Mater* 18:2379–2383
- Algadi H, Das T, Ren J, Li H (2023) High-performance and stable hybrid photodetector based on a monolayer molybdenum disulfide (MoS_2)/nitrogen doped graphene quantum dots (NH_2 GQDs)/all-inorganic (CsPbBr_3) perovskite nanocrystals triple junction. *Adv Compos Hybrid Mater* 6:56
- Algadi H, Ren J, Alqarni A (2023) A high-performance self-powered photodetector based on solution-processed nitrogen-doped graphene

- quantum dots/all-inorganic perovskite heterostructures. *Adv Compos Hybrid Mater* 6:98
25. Xue DJ, Wang JJ, Wang YQ, Xin S, Guo YG, Wan LJ (2011) Facile synthesis of germanium nanocrystals and their application in organic–inorganic hybrid photodetectors. *Adv Mater* 23:3704–3707
 26. Zhai T, Li L, Ma Y, Liao M, Wang X, Fang X et al (2011) One-dimensional inorganic nanostructures: synthesis, field-emission and photodetection. *Chem Soc Rev* 40:2986–3004
 27. Pron A, Rannou P (2002) Processible conjugated polymers: from organic semiconductors to organic metals and superconductors. *Prog Polym Sci* 27:135–190
 28. Che Y, Yang X, Liu G, Yu C, Ji H, Zuo J et al (2010) Ultrathin n-type organic nanoribbons with high photoconductivity and application in optoelectronic vapor sensing of explosives. *J Am Chem Soc* 132:5743–5750
 29. Adepu V, Kunchur A, Kolli CSR, Siddhartha S, Mattela V, Sahatiya P (2022) High-performance visible light photodetector based on 1D SnO₂ nanofibers with a Ti₃C₂T_x (MXene) electron transport layer. *ACS Appl Nano Mater*
 30. Aggarwal P, Kaushik S, Bisht P, Sharma M, Singh A, Mehta BR et al (2022) Centimeter-scale synthesis of monolayer WS₂ using single-zone atmospheric-pressure chemical vapor deposition: a detailed study of parametric dependence, growth mechanism, and photodetector properties. *Cryst Growth Des* 22:3206–3217
 31. Agrohiya S, Kumar V, Rawal I, Dahiya S, Goyal PK, Kumar V (2022) Fabrication of n-TiO₂/p-Si photo-diodes for self-powered fast ultraviolet photodetectors. *Silicon* 1–11
 32. Yin Z, Li H, Li H, Jiang L, Shi Y, Sun Y et al (2012) Single-layer MoS₂ phototransistors. *ACS Nano* 6:74–80
 33. Singh A, Verma A, Yadav B, Chauhan P (2022) Earth-abundant and environmentally benign Ni–Zn iron oxide intercalated in a polyaniline based nanohybrid as an ultrafast photodetector. *Dalton Trans* 51:7864–7877
 34. Singh A, Chauhan P, Verma A, Chandra Yadav B (2023) CuBi₂O₄ nanocrystals integrated with polyaniline nanobelt arrays for weak light photomultiplication type photodetector. *Sustain Energy Fuels*
 35. Lim BT, Kang I, Kim CM, Kim SY, Kwon S-K, Kim Y-H et al (2014) Solution-processed high-performance photodetector based on a new triisopropylsilylethynyl anthracene derivative. *Org Electron* 15:1856–1861
 36. Jin Z, Wang J (2014) PIN architecture for ultrasensitive organic thin film photoconductors. *Sci Rep* 4:1–7
 37. Li L, Zhang F, Wang W, Fang Y, Huang J (2015) Revealing the working mechanism of polymer photodetectors with ultrahigh external quantum efficiency. *Phys Chem Chem Phys* 17:30712–30720
 38. Chen H, Yu P, Zhang Z, Teng F, Zheng L, Hu K et al (2016) Ultrasensitive self-powered solar-blind deep-ultraviolet photodetector based on all-solid-state polyaniline/MgZnO bilayer. *Small* 12:5809–5816
 39. Talib RA, Abdullah M, Al-Salman HS, Mohammad SM, Allam NK (2016) ZnO nanorods/polyaniline heterojunctions for low-power flexible light sensors. *Mater Chem Phys* 181:7–11
 40. Verma A, Chaudhary P, Singh A, Tripathi RK, Yadav B (2022) ZnS nanosheets in a polyaniline matrix as metallopolymer nanohybrids for flexible and biofriendly photodetectors. *ACS Applied Nano Materials* 5:4860–4874
 41. Alruqi M, Rabia M, Elsayed AM, Hanafi HA, Shaban M, Abdel Hamid MM (2023) Development of polypyrrole/Ni(OH)₂-NiO core-shell nanocomposite as an optoelectronic device. *J Appl Polym Sci* 140:e53833
 42. Briseno AL, Holcombe TW, Boukai AI, Garnett EC, Shelton SW, Fréchet JJ et al (2010) Oligo- and polythiophene/ZnO hybrid nanowire solar cells. *Nano Lett* 10:334–340
 43. Wang X, Song W, Liu B, Chen G, Chen D, Zhou C et al (2013) High-performance organic-inorganic hybrid photodetectors based on P3HT: CdSe nanowire heterojunctions on rigid and flexible substrates. *Adv Func Mater* 23:1202–1209
 44. Fan G, Wang Z, Ren H, Liu Y, Fan R (2021) Dielectric dispersion of copper/rutile cermets: dielectric resonance, relaxation, and plasma oscillation. *Scripta Mater* 190:1–6
 45. Fan G, Wang Z, Sun K, Liu Y, Fan R (2021) Doped ceramics of indium oxides for negative permittivity materials in MHz-kHz frequency regions. *J Mater Sci Technol* 61:125–131
 46. Xie P, Zhang Z, Liu K, Qian L, Dang F, Liu Y et al (2017) C/SiO₂ meta-composite: overcoming the λ/a relationship limitation in metamaterials. *Carbon* 125:1–8
 47. Hao Y, Leng Z, Yu C, Xie P, Meng S, Zhou L et al (2023) Ultralightweight hollow bowl-like carbon as microwave absorber owning broad band and low filler loading. *Carbon* 212:118156
 48. K Sharma A, Chaudhary G, Bhardwaj P, Kaushal I, Duhan S (2017) Studies on metal doped polyaniline-carbon nanotubes composites for high performance supercapacitor. *Curr Anal Chem* 13:277–284
 49. Vyas S, Shukla A, Shivhare S, Das R, Venkatesh R (2023) Core-shell structured polyaniline (PANI)–manganese dioxide (MnO₂) nanocomposites as an electrochemical sensor for detection of emamectin benzoate. *ES Mater Manuf* 23:1002
 50. Zhu Q, Gao F, Yang Y, Zhang B, Wang W, Hu Z et al (2015) Electrochemical preparation of polyaniline capped Bi₂S₃ nanocomposite and its application in impedimetric DNA biosensor. *Sens Actuators, B Chem* 207:819–826
 51. Singh A, Chauhan P, Verma A, Yadav B (2023) An investigation into the hybrid architecture of Mn–Co nanoferrites incorporated into a polyaniline matrix for photoresponse studies. *Phys Chem Chem Phys* 25:21383–21396
 52. Singh A, Chauhan P (2023) WS₂–polyaniline nanohybrid materials for high-external quantum efficiency photoelectric devices utilized in flexible electronics. *ACS Appl Opt Mater* 2:28–40
 53. Paul S, Karthikeyan B (2022) Tailoring exciton diffusion length in ZnO@ mos2 core-shell/polyaniline nanocomposite films and photocurrent generation applications. *ACS Appl Nano Mater* 5:16116–16125
 54. Carrano JC, Li T, Grudowski PA, Eiting CJ, Dupuis RD, Campbell JC (1998) Current transport mechanisms in GaN-based metal–semiconductor–metal photodetectors. *Appl Phys Lett* 72:542–544
 55. Yadav G, Gupta V, Tomar M (2022) Double Schottky metal–semiconductor–metal based GaN photodetectors with improved response using laser MBE technique. *J Mater Res* 37:457–69
 56. Patel M, Song J, Kim D-W, Kim J (2022) Carrier transport and working mechanism of transparent photovoltaic cells. *Appl Mater Today* 26:101344
 57. Shi L, Chen K, Zhai A, Li G, Fan M, Hao Y et al (2021) Status and outlook of metal–inorganic semiconductor–metal photodetectors. *Laser Photonics Rev* 15:2000401
 58. Kumawat KL, Singh DK, Nanda KK, Krupanidhi SB (2021) Solution-processed SnSe₂–RGO-based bulk heterojunction for self-powered and broadband photodetection. *ACS Appl Electron Mater* 3:3131–3138
 59. Sun Y, Song W, Gao F, Wang X, Luo X, Guo J et al (2020) In situ conformal coating of polyaniline on GaN microwires for ultrafast, self-driven heterojunction ultraviolet photodetectors. *ACS Appl Mater Interfaces* 12:13473–13480
 60. Yu P, Hu K, Chen H, Zheng L, Fang X (2017) Novel p–p heterojunctions self-powered broadband photodetectors with ultrafast speed and high responsivity. *Adv Func Mater* 27:1703166
 61. Kannichankandy D, Pataniya PM, Zankat CK, Tannarana M, Pathak VM, Solanki GK et al (2020) Paper based organic–inorganic hybrid photodetector for visible light detection. *Appl Surf Sci* 524:146589

62. Yan T, Cai S, Hu Z, Li Z, Fang X (2021) Ultrafast speed, dark current suppression, and self-powered enhancement in TiO₂-based ultraviolet photodetectors by organic layers and Ag nanowires regulation. *J Phys Chem Lett* 12:9912–9918
63. Wang Y, Li L, Wang H, Su L, Chen H, Bian W et al (2020) An ultrahigh responsivity self-powered solar-blind photodetector based on a centimeter-sized β-Ga₂O₃/polyaniline heterojunction. *Nanoscale* 12:1406–1413
64. Zheng L, Yu P, Hu K, Teng F, Chen H, Fang X (2016) Scalable-production, self-powered TiO₂ nanowell–organic hybrid UV photodetectors with tunable performances. *ACS Appl Mater Interfaces* 8:33924–33932
65. Sharma S, Kumar D, Khare N (2021) Three-dimensional hierarchical PANI/Bi₂S₃ nanoflowers heterojunction for enhanced photoelectrochemical water splitting. *J Alloy Compd* 865:158779
66. Subramanian S, Padiyan DP (2009) Inclusion of polyaniline in electrodeposited bismuth sulphide thin films: synthesis and characterization. *Curr Appl Phys* 9:1140–1145
67. Purohit S, Yadav KL, Satapathi S (2022) Metal halide perovskite heterojunction for photocatalytic hydrogen generation: progress and future opportunities. *Adv Mater Interfaces* 9:2200058
68. Wang C-H, Qin D-D, Shan D-L, Gu J, Yan Y, Chen J et al (2017) Assembly of g-C₃N₄-based type II and Z-scheme heterojunction anodes with improved charge separation for photoelectrojunction water oxidation. *Phys Chem Chem Phys* 19:4507–4515
69. Khalid N, Hussain MK, Murtaza G, Ikram M, Ahmad M, Hammad A (2019) A novel Ag₂O/Fe–TiO₂ photocatalyst for CO₂ conversion into methane under visible light. *J Inorg Organomet Polym Mater* 29:1288–1296
70. Khalid N, Arshad A, Tahir M, Hussain MK (2021) Fabrication of p–n heterojunction Ag₂O@Ce₂O nanocomposites make enables to improve photocatalytic activity under visible light. *Appl Nanosci* 11:199–206
71. Mitra M, Ghosh A, Mondal A, Kargupta K, Ganguly S, Banerjee D (2017) Facile synthesis of aluminium doped zinc oxide-polyaniline hybrids for photoluminescence and enhanced visible-light assisted photo-degradation of organic contaminants. *Appl Surf Sci* 402:418–428
72. Hussain MK, Khalid N (2022) Surfactant-assisted synthesis of MoO₃ nanorods and its application in photocatalytic degradation of different dyes in aqueous environment. *J Mol Liq* 346:117871
73. Hussain MK, Khalid N, Tanveer M, Kebaili I, Alrobei H (2022) Fabrication of CuO/MoO₃ pn heterojunction for enhanced dyes degradation and hydrogen production from water splitting. *Int J Hydrogen Energy* 47:15491–15504
74. Rahman KH, Kar AK (2020) Effect of band gap variation and sensitization process of polyaniline (PANI)-TiO₂ pn heterojunction photocatalysts on the enhancement of photocatalytic degradation of toxic methylene blue with UV irradiation. *J Environ Chem Eng* 8:104181
75. Yang H, Wan Y, Cheng Q, Zhou H, Pan Z (2022) Enhanced photocatalytic performance over PANI/NH₂-MIL-101 (Fe) with tight interfacial contact. *Dalton Trans* 51:15080–15088
76. Khalid N, Hammad A, Tahir M, Rafique M, Iqbal T, Nabi G et al (2019) Enhanced photocatalytic activity of Al and Fe co-doped ZnO nanorods for methylene blue degradation. *Ceram Int* 45:21430–21435
77. Hussain MK, Khalid N, Tahir M, Tanveer M, Iqbal T, Liaqat M (2023) Enhanced visible light-driven photocatalytic activity and stability of novel ternary ZnO/CuO/MoO₃ nanorods for the degradation of rhodamine B and alizarin yellow. *Mater Sci Semicond Process* 155:107261
78. Azadinia M, Fathollahi M, Mosadegh M, Boroumand F, Mohajeri E (2017) Improved performance of photoconductive gain hybrid UV detector by trap state engineering of ZnO nanoparticles. *J Appl Phys* 122:154501
79. Röhr JA, Moia D, Haque SA, Kirchartz T, Nelson J (2018) Exploring the validity and limitations of the Mott–Gurney law for charge-carrier mobility determination of semiconducting thin-films. *J Phys: Condens Matter* 30:105901
80. Zou C, Liu Q, Chen K, Chen F, Zhao Z, Cao Y et al (2022) A high-performance polarization-sensitive and stable self-powered UV photodetector based on a dendritic crystal lead-free metal-halide CsCu₂I₃/GaN heterostructure. *Mater Horiz* 9:1479–1488
81. Algadi H, Ren J, Alqarni A (2023) Solution-processed nitrogen-doped graphene quantum dots/perovskite composite heterojunction for boosting performance of anatase titanium dioxide (TiO₂)-based UV photodetector. *Adv Compos Hybrid Mater* 6:86
82. Kumar V, Rawal I, Kumar V, Goyal PK (2019) Efficient UV photodetectors based on Ni-doped ZnS nanoparticles prepared by facial chemical reduction method. *Physica B* 575:411690
83. Ye Z, Xie S, Cao Z, Wang L, Xu D, Zhang H et al (2021) High-rate aqueous zinc-organic battery achieved by lowering HOMO/LUMO of organic cathode. *Energy Storage Materials* 37:378–386
84. Bhadra S, Khastgir D, Singha NK, Lee JH (2009) Progress in preparation, processing and applications of polyaniline. *Prog Polym Sci* 34:783–810
85. Zujovic ZD, Laslau C, Bowmaker GA, Kilmartin PA, Webber AL, Brown SP et al (2010) Role of aniline oligomeric nanosheets in the formation of polyaniline nanotubes. *Macromolecules* 43:662–670
86. Djurovich PI, Mayo EI, Forrest SR, Thompson ME (2009) Measurement of the lowest unoccupied molecular orbital energies of molecular organic semiconductors. *Org Electron* 10:515–520
87. Özcan M, Dehri İAS, Erbil M (2004) Organic sulphur-containing compounds as corrosion inhibitors for mild steel in acidic media: correlation between inhibition efficiency and chemical structure. *Appl Surf Sci* 236:155–164

Publisher's Note Springer Nature remains neutral with regard to jurisdictional claims in published maps and institutional affiliations.

Springer Nature or its licensor (e.g. a society or other partner) holds exclusive rights to this article under a publishing agreement with the author(s) or other rightsholder(s); author self-archiving of the accepted manuscript version of this article is solely governed by the terms of such publishing agreement and applicable law.